doi:10.26443/seismica.v3i2.1351

Heterogeneous high frequency seismic radiation from complex ruptures

Sara B. L. Cebry [*1], **Gregory C. McLaskey** [2]

[1]Civil and Environmental Engineering, Cornell University, Ithaca, NY, USA; Now at USGS, Moffett Field, CA, USA, [2]Civil and Environmental Engineering, Cornell University, Ithaca, NY, USA

Author contributions: *Conceptualization*: S. B. L. Cebry, G. C. McLaskey. *Formal Analysis*: S.B.L. Cebry. *Writing - Original draft*: S. B. L. Cebry. *Writing - Review & Editing*: S. B. L. Cebry, G. C. McLaskey. *Funding acquisition*: G. C. McLaskey.

Abstract Fault geometric heterogeneities such as roughness, stepovers, or other irregularities are known to affect the spectra of radiated waves during an earthquake. To investigate the effect of normal stress heterogeneity on radiated spectra, we utilized a poly(methyl methacrylate) (PMMA) laboratory fault with a single, localized bump. By varying the normal stress on the bump and the fault-average normal stress, we produced earthquake-like ruptures that ranged from smooth, continuous ruptures to complex ruptures with variable rupture propagation velocity, slip distribution, and stress drop. High prominence bumps produced complex events that radiated more high frequency energy, relative to low frequency energy, than continuous events without a bump. In complex ruptures, the high frequency energy showed significant spatial variation correlated with heterogeneous peak slip rate and maximum local stress drop caused by the bump. Continuous ruptures emitted spatially uniform bursts of high frequency energy. Near-field peak ground acceleration (PGA) measurements of complex ruptures show nearly an order-of-magnitude higher PGA near the bump than elsewhere. We propose that for natural faults, geometric heterogeneities may be a plausible explanation for commonly observed order-of-magnitude variations in near-fault PGA.

Resumen (Translated by Coralis Del Mar Friedman-Álvarez) Durante un terremoto, las heterogeneidades geométricas en fallas, incluyendo asperidad, escalonamientos y otras irregularidades, afectan los espectros de las ondas radiadas. Para investigar el efecto de la heterogeneidad del esfuerzo normal sobre los espectros radiados, utilizamos una falla de laboratorio hecha de polimetilmetacrilato (PMMA) con una protuberancia localizada. Al variar el esfuerzo normal sobre la protuberancia y el esfuerzo normal promedio de la falla, produjimos rupturas similares a las que ocurren en terremotos, variando desde rupturas suaves y continuas hasta rupturas complejas, con variaciones en la velocidad de propagación de ruptura, distribución de deslizamiento y caída de esfuerzo. Al comparar los eventos producidos por protuberancias prominentes con los eventos continuos sin protuberancia, se observa que las protuberancias prominentes generan eventos más complejos que radian más energía de alta frecuencia en comparación con la energía de baja frecuencia. En rupturas complejas, la energía de alta frecuencia muestra una variación espacial significativa, correspondiente a la variación de la tasa máxima de deslizamiento y la caída máxima de esfuerzo local causadas por la protuberancia, mientras que las rupturas continuas emiten pulsos uniformes de energía de alta frecuencia. En rupturas complejas, la energía de alta frecuencia muestra una variación espacial significativa. Esta variación corresponde con la variabilidad en la tasa máxima de deslizamiento y la caída máxima de esfuerzo local, las cuales son causadas por la protuberancia. En contraste, las rupturas continuas emiten pulsos uniformes de energía de alta frecuencia. Las medidas de Aceleración Máxima del Suelo (PGA, por sus siglas en inglés) de rupturas complejas en el campo cercano son un orden de magnitud más altas cerca de la protuberancia que en otras partes de la falla. Proponemos que heterogeneidades geométricas en fallas naturales podrían explicar las variaciones de un orden de magnitud comúnmente observadas en la PGA cercana a la falla.

Production Editor:
Hannah Mark
Handling Editor:
Matt Ikari
Copy & Layout Editor:
Miguel Neves

Signed reviewer(s):
Marco Scuderi

Received:
April 9, 2024
Accepted:
August 9, 2024
Published:
September 17, 2024

*Corresponding author: sarabethleach@gmail.com

Non-technical summary Faults in the earth are not perfectly flat or uniform, which makes it difficult to predict how much damage an earthquake will cause. Infrastructure is designed to withstand earthquakes using a parameter called Peak Ground Acceleration (PGA) which characterizes how much high frequency shaking a specific location will experience. Several factors determine PGA including site and path effects, and source parameters. In this study we investigate how a 0.74 m PMMA fault with a single bump affects the resulting shaking. In our experiments, the area with the bump was pressed together harder than the surrounding fault and produced a non-uniform normal stress distribution. We found that this created a region with enhanced high frequency radiation and near-field PGA, nearly an order-of-magnitude higher than elsewhere. Even far away from the bump, the PGA was higher than PGA on a uniform fault without a bump, even though the overall size of the event was similar. As the size of the bump increased relative to the rest of the fault, the enhanced PGA also increased. We think non-uniform faults may be one explanation for natural observations of areas with persistent high PGA.

Resumen no técnico (Translated by Coralis Del Mar Friedman-Álvarez) Las fallas en la Tierra no son perfectamente planas o uniformes, lo cual dificulta predecir cuánto daño podría provocar un terremoto. La infraestructura está diseñada para resistir terremotos utilizando un parámetro denominado Aceleración Máxima del Suelo (PGA, por sus siglas en inglés), que caracteriza cuánto movimiento sísmico de alta frecuencia experimentará un lugar en particular. Varios factores determinan la PGA, incluyendo los efectos de sitio, la trayectoria de la onda sísmica, y los parámetros del origen. En este estudio investigamos experimentalmente el efecto sísmico producido al agregar una protuberancia en el plano de una falla de polimetilmetacrilato de 0.74 m. En nuestros experimentos, el área con la protuberancia fue presionada con mayor fuerza que el área circundante de la falla, produciendo una distribución no uniforme del esfuerzo normal. Esto crea una región de radiación de alta frecuencia intensificada, y una PGA en campo cercano casi un orden de magnitud mayor que en otras partes. Incluso lejos de la protuberancia, la PGA medida fue mayor que en una falla uniforme sin protuberancia, aunque el tamaño total del evento fue similar. A medida que aumentaba el tamaño de la protuberancia en relación al resto de la falla, también aumentaba la PGA intensificada. Pensamos que las fallas no uniformes podrían ser una explicación para observaciones naturales de áreas con PGA persistentemente alta.

1 Introduction

To prevent earthquake damage to infrastructure, ground motions must be accurately predicted, particularly at high frequencies (0.2-10 Hz) which produce the largest accelerations that damage buildings. High frequency earthquake ground motions are characterized by the peak ground acceleration (PGA) which is used to design infrastructure to withstand earthquake hazards. However, PGA is difficult to predict due to large influence from earthquake source parameters. Source details such as rupture speed (Bao et al., 2019), direction (Courboulex et al., 2013), and slip distribution (Miyake, 2003) can create heterogeneous near-fault PGAs. For example, the 2023 Kahramanmaraş earthquakes produced an order-of-magnitude variation in PGA along the fault (Mai et al., 2023). Site and path effects also heavily influence PGA, however these spatial variations in near-fault PGA as well as stress drop and high frequency spectral decay can persist over multiple earthquakes (Trugman and Shearer, 2017; Tsurugi et al., 2020) even when path and site effects are removed.

The theoretical predictions of high frequency radiation due to fault heterogeneities are supported by modeling studies. There are several studies that suggest an increase in high frequency radiation from fault heterogeneity such as fault kinks (Madariaga et al., 2006), high strength barriers (Das and Aki, 1977; Dunham et al., 2003), fault roughness (Shi and Day, 2013; Dunham et al., 2011), or initial stress heterogeneity (Oral et al., 2022). In many cases, the heterogeneity caused a change in rupture velocity, which in turn caused variations in fault slip velocity which radiated high frequency energy (Madariaga, 1976). Experimental studies have shown similar variations in slip velocity due to kinks (Rousseau and Rosakis, 2003), bumps (Cebry et al., 2023), stress variations (Cebry et al., 2022a,b) and frictional properties (Buijze et al., 2021; Rubino et al., 2022; Yamashita et al., 2021).

Source spectra of laboratory slip events has been investigated for idealized smooth, flat faults for slow and fast earthquakes with magnitudes ranging from M −7.5 to M −2.5 (McLaskey and Yamashita, 2017; Wu and McLaskey, 2019). Selvadurai (2019) also looked at source spectra of smaller laboratory earthquakes (M −9 to M −7.5) and provided links between laboratory and natural seismicity. Similar to natural events, these simple, continuous laboratory earthquakes can be roughly fit with a Brune-type spectra model with a single corner frequency and high frequency fall off rate ranging from ω^{-1} (for slow events) (Wu and McLaskey, 2019) to around ω^{-2} (for fast events) (McLaskey and Yamashita, 2017) with some events reaching up to $\omega^{-3.5}$ (Selvadurai, 2019). Other studies looked at how spatially averaged radiated waves varied as a function of average rupture velocity or stress conditions (McLaskey and Lockner, 2018; Marty et al., 2019).

To investigate the effect of fault heterogeneity on ra-

diated spectra, we used a 0.74 m fault with a 0.025 m long bump of locally high normal stress. Experimental methods and governing fault mechanics were presented in an earlier study (Cebry et al., 2023). In this work we conducted additional experiments and analysis, focused on the radiation of seismic waves and near-field PGA. By varying the bump prominence (normal stress on the bump above the sample-average normal stress, $\Delta\sigma_b$ / sample-average normal stress, $\overline{\sigma_n}$), we produced both consistent and variable sequences of earthquake-like ruptures on the same laboratory fault. In consistent sequences, each event had a continuous rupture front that propagated from one end of the fault to the other. Variable sequences were made up of partial and complex events. Partial events only ruptured a portion of the fault while other fault sections remained locked. Complex events ruptured the entire fault and had local variations in propagation velocity, slip distribution, and stress drop. Continuous ruptures emitted spatially uniform high frequency energy near the rupture tip while complex ruptures showed significant spatial variation in the amplitude and timing of high frequency energy radiation with more high frequency energy relative to low frequency energy overall. High frequency energy was spatio-temporally correlated with the rupture front and spatially correlated with peak slip rate and local stress drop. We propose that on natural faults, fault geometric heterogeneities can be a source of enhanced, spatially heterogeneous high frequency radiation. In areas of enhanced high frequency radiation, this can result in PGAs that are larger than predicted and cause increased damage to infrastructure.

2 Methods

We used a biaxial load frame to squeeze two built-up blocks of poly(methyl methacrylate) (PMMA), (referred to as the moving and stationary block, Figure 1a) together at a constant $\overline{\sigma_n}$. The moving and stationary blocks were made up of 30 and 32 PMMA "sub-blocks" held together with tensioned steel rods in the x-direction (Figure S1). The moving block was 740 by 200 by 38 mm in the x, y, z directions, the stationary block was 778 by 149 by 38 mm. The sub-blocks could slip in the y-direction to accommodate large changes in local normal stress, while still held together in the x-direction so each composite block behaved similar to an intact, homogenous block (Cebry et al., 2023).

The sample was outfitted with an array of sensors to measure ground motions and apparent slip at eight points along the fault. Eight Panametrics V103, 13 mm diameter piezoelectric sensors (PZ) were used to measure vertical ground motions with a minimum resolution of 6.3 mV. The PZ frequency response spectra is approximately flat between 30 and 400 kHz. Below 10 kHz, the response falls off at a rate of 40 dB/decade (Wu and McLaskey, 2018). This provides a minimum displacement resolution of approximately 0.63 nm in the 30 - 400 kHz frequency band. Sensors were attached with hot glue to the moving block 3.5 cm from the fault in the y-direction at 3.75 cm, 20.5 cm, 40.5 cm, and 60.75 cm in the x-direction and attached to the stationary block −3.1 cm from the fault in the y-direction at 11 cm, 30.3 cm, 52.5 cm, and 69.5 cm in the x-direction (Figure 1). PZ sensors were placed such that the entire sensor was attached to a single sub-block. Signals were recorded directly using an Elsys TraNET digitizer with no additional amplifier or filter.

Eight eddy current displacement sensors were placed on the fault, co-located with the PZ sensors in the x-direction to measure apparent fault slip to a 0.15 µm precision. We use the term "apparent slip" to distinguish between true slip on the fault and slip measured between the sensor probe and target which may also include strain changes due to a slight offset in the x and y-direction. Both PZ and apparent slip measurements were continuously recorded at 5 kHz and also at 5 MHz for 0.08 s time windows centered around slip events. Figure 2a shows an example of the raw data recorded by the PZ sensors, offset by distance along the fault.

In each experimental run, steel shims (25 x 0.838 x 38 mm) were placed at x = 32 cm between one of the sub-blocks and the load frame to create a bump with normal stress equal to σ_b following the procedure of Cebry et al. (2023). The $\overline{\sigma_n}$ was increased to a prescribed level and held constant. Then sample-average shear stress was increased at a constant displacement rate of approximately 0.54 MPa/min or 4.3 µm/s. Slip occurred on the simulated 38 mm x 740 mm fault interface between the two blocks and on a low friction interface between the moving block and the steel frame (Figure 1a). Experimental runs were conducted at 2 MPa, 4 MPa, and 8 MPa $\overline{\sigma_n}$ with zero ($\Delta\sigma_b$ = 0 MPa), two ($\Delta\sigma_b$ = 12.5 MPa), four ($\Delta\sigma_b$ = 25.0 MPa), or six shims ($\Delta\sigma_b$ = 37.4 MPa) which provided an order-of-magnitude variation in bump prominence ($\Delta\sigma_b/\overline{\sigma_n}$, Figure S2). At each set of experimental conditions, we produced a series of five sample-spanning, stick-slip events. All events reported here occurred after a run-in period, during which the sample was sheared under experimental conditions. The run-in phase was complete once the sample produced regular sequences of stick-slip events. This procedure relieved stresses built up between the sub-blocks and on the fault during the initial increase in $\overline{\sigma_n}$ due to the shims and rotation of the sub-blocks.

2.1 Calibration of piezoelectric sensors

To quantify the absolute event magnitude and determine the source spectra of radiated seismic waves, we used an empirical Green's function (EGF) method with ball impacts and a small slip event as EGF sources (McLaskey et al., 2015; Wu and McLaskey, 2019). This method characterizes the path, coupling method, instrument response, apparatus effect, and recording system together as one signal, so that the source spectra can be deconvolved from the raw signal in one step. For the ball impacts, we dropped 1 mm and 2.38 mm diameter steel balls from 1 m above the top of the sample loaded at 4 MPa $\overline{\sigma_n}$ with six shims. For the small event we used a partially confined event from an experiment at 2 MPa $\overline{\sigma_n}$. The signals were recorded under the same conditions as the experiments, then transformed into the Fourier domain, averaged across all eight PZ sen-

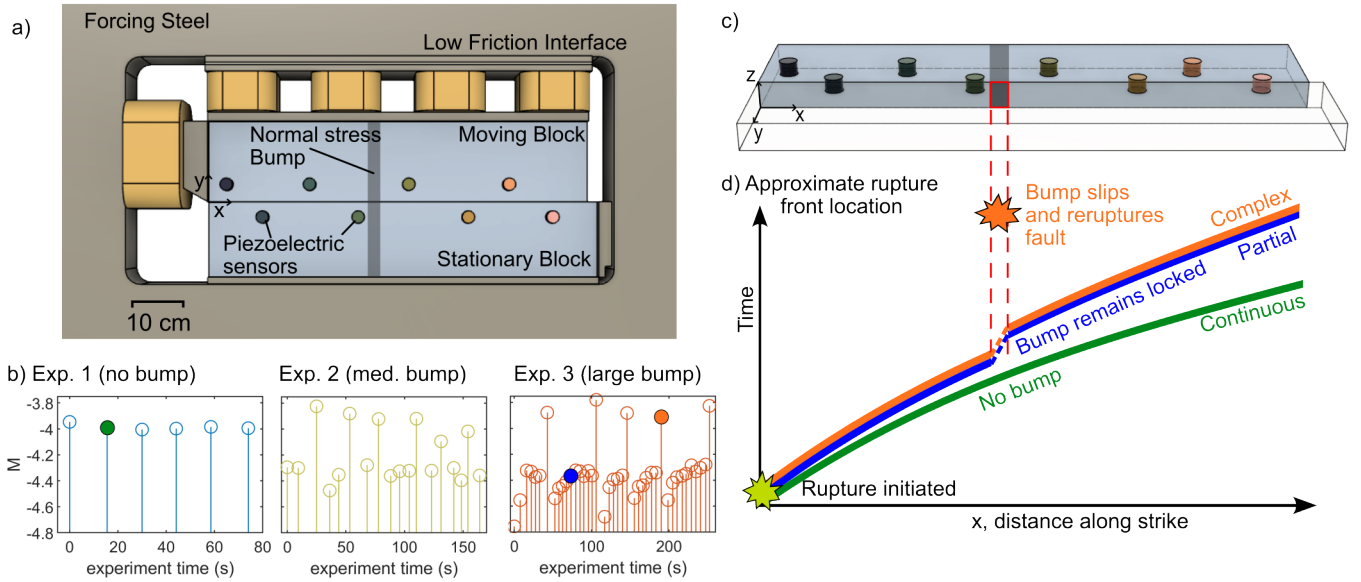

Figure 1 a) Schematic of loading apparatus with sample (blue rectangles) and piezoelectric sensors (small circles). Grey shaded area on the samples represents the portion of the sample with increased normal stress in some experiments. b) Moment magnitude of three experiments with bump prominence of 0 (no bump), 12.5 (medium bump), and 18.7 (large bump), all conducted with $\overline{\sigma_n} = 2$ MPa. Filled circles indicate the three representative events. c) Schematic of the samples looking onto the fault with the locations of piezoelectric sensors marked by colored cylinders. The shaded area and red square mark the location of the bump for the partial and complex ruptures. d) Rupture front location as a function of space and time for the continuous (green), partial (blue), and complex (orange) events based on slip measurements.

sors, and concatenated over frequency bands that were both below the corner frequency (f_c) of each source and possessed good signal-to-noise ratio (Figure S3). This method allowed us to achieve an EGF spectrum with a broad frequency range (10^2 to 10^5 Hz).

For the individual events, source spectra were calculated from a 0.08 s window of vertical ground motions (Figure 2a). The raw signals were Fourier transformed into the frequency domain (Figure S4) then averaged across all eight sensors (Figure 2b). The averaged raw spectra were divided by the EGF spectrum (Figure S3). We choose to average the spectra across the eight PZ sensors prior to removal of the instrument-apparatus response to reduce the effect of different source-to-sensor paths for the ball impacts and the seismic sources.

To determine PGA, raw individual sensor measurements were converted to a displacement using the calibration factor of 0.01 V/nm (McLaskey and Glaser, 2010; Wu and McLaskey, 2018) between 10^4 and 10^5 Hz. In this frequency band, the instrument frequency response is flat so the sensor is measuring ground displacement rather than acceleration or velocity and our measurements have good signal to noise ratio. Acceleration was derived from displacement and the maximum of each sensor was taken to be the PGA at that location. Site and path effects were not removed from this measurement but did remain constant for each event and each experiment, so differences in PGA are only due to source effects.

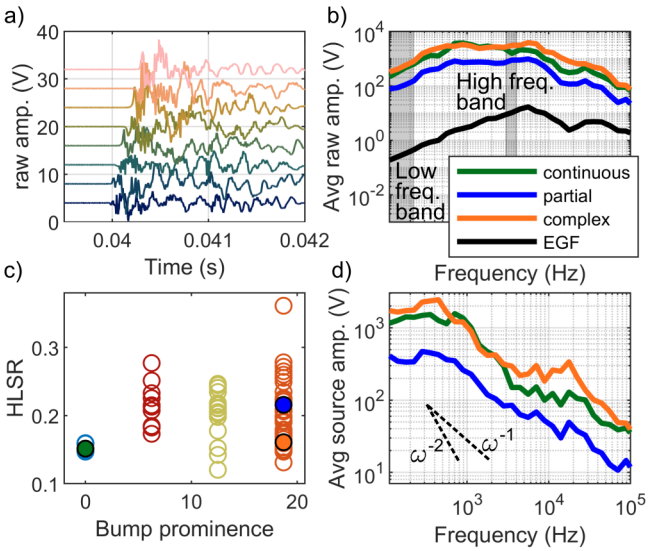

Figure 2 a) Raw data recorded from eight piezoelectric sensors offset for clarity. b) Fourier spectra, averaged across eight piezoelectric sensors for three rupture events and empirical Green's function. Grey shaded regions show the frequency bins used for comparison across events and experiments in c). c) High-to-low spectral ratio between 2.8 and 4 kHz (high frequency) divided by spectra amplitude between 110 and 220 Hz (low frequency) for each event from four different experiments at 2 MPa $\overline{\sigma_n}$ with varied bump prominence. d) Calibrated source spectra determined using the EGF shown in b).

3 Results

Bump prominence had a significant effect on the radiated seismic waves. Slip events that were more complex

with variable rupture propagation velocity, slip distribution, and stress drop, radiated more high frequency energy than continuous ruptures and had spatially heterogeneous high frequency energy and PGA.

To illustrate these differences, throughout the paper we compare three representative events from experiments at 2 MPa $\overline{\sigma_n}$ with different rupture behavior (Figure 1d). The first representative event is a "continuous" rupture from an experiment with a $\Delta\sigma_b/\overline{\sigma_n}$=0 which smoothly propagated at a constant rate along the entire fault with no pauses (Figure 1d in green, and Figure S5a,d).

The second and third representative events, a "partial" and "complex" rupture, are from an experiment with a prominent bump ($\Delta\sigma_b/\overline{\sigma_n}$=18.7). Increased $\Delta\sigma_b/\overline{\sigma_n}$, promoted variable rupture sequences comprised of events with variable rupture length, slip amount, and magnitude (Figure 1b and S2). The partial rupture slipped the first 31 cm of the fault before pausing briefly (0.03 ms). After this pause the rupture re-initiated on the other side of the bump and continued to rupture the rest of the fault while the bump remained locked (Figure 1d in blue and Figure S5b,e). The complex rupture began the same as the partial event, but 0.34 ms after rupture initiated, the bump slipped and re-ruptured the entire fault (Figure 1d in orange, and Figure S5c,e).

The differences between the partial and complex ruptures are due to differences in strength excess on the bump (Cebry et al., 2023). For example, the partial rupture occurred when the bump had a lower initial shear stress at the start of rupture, and therefore a larger strength excess. This is nearly the same as the case of a rupture "skipping past" a barrier, described by Das and Aki (1977) (Case P-SV-1). The complex rupture occurred when the bump had a higher initial shear stress. When the bump finally slipped it provided ample fuel to rerupture the entire fault. This is similar to the case from Das and Aki (1977), where two barriers are "eventually broken" (Case P-SV-4), although in our case there is only one barrier. Note that as normal stress is increased, the strength excess on the bump, and therefore the stress on the bump ($\Delta\sigma_b$) required to stop ruptures increased. With smaller variations in strength excess along the fault, ruptures become less complex. A higher normal stress with the same bump size will result in less complex ruptures compared to a lower normal stress (Cebry et al., 2023). We were unable to compare complete, partial, and complex ruptures at higher normal stress, since the creation of a bump with sufficiently large $\Delta\sigma_b$ to consistently stop ruptures was not experimentally achievable in our set up at or above 8 MPa normal stress.

3.1 Radiated spectra

We compare the spectra from the three representative events and find that the complex and continuous ruptures are both larger than the partial rupture across all frequency bands, but the partial rupture has enhanced high frequency energy relative to low frequency energy (Figure 2). The complex event also had enhanced energy in the 3 - 10 kHz range compared to the continuous event. To compare directly across events and experiments, we took the average amplitude in a high frequency bin (2.8 - 4 kHz) normalized by the average amplitude in a low frequency bin (110 - 220 Hz) for each individual event. The low frequency bin was chosen to be below the expected corner frequency for all events and is thus related to the seismic moment. The high frequency bin was chosen to be above the expected corner frequency for all events. It was also chosen to avoid variations in sensor sensitivity between 10 and 20 kHz (Wu and McLaskey, 2018), where the sensor measurement transitions from acceleration to displacement. We will refer to this value as the high-to-low spectral ratio (HLSR). HLSR can be thought of as how much high frequency energy is released relative to low frequencies where we measure magnitude and event size. In this sense, HLSR is akin to seismic stress drop. Since high frequency energy is what causes the most damage to infrastructure, this parameter can be thought of as the potential for damage relative to magnitude.

Comparison across all experimental runs and events confirms that experiments with higher bump prominence had a larger range of HLSR and a higher maximum HLSR (Figure 2c). Events with the highest HLSR were typically similar to the representative partial rupture. These events were most common at 2 MPa $\overline{\sigma_n}$ with 6 shims. However, complex rupture behavior was not a requirement for increased HLSR. Even at 8 MPa $\overline{\sigma_n}$ where all ruptures were continuous, complete ruptures, higher bump prominence resulted in higher HLSR, although to a lesser degree than at 2 MPa $\overline{\sigma_n}$ (Figure S6).

Figure 2d shows the source spectra for the three representative events with path, instrument, and recording system effects removed. The spectra were then fit with a Brune-type source model (Brune, 1970; Kaneko and Shearer, 2015) with a high frequency fall off of ω^{-1} (Figure S7) over a frequency range of 10^2 to 10^5 Hz. Moment was chosen based on low frequencies (110 - 220 Hz), then the corner frequency was chosen to reduce the mean absolute error. Continuous, partial, and complex ruptures had moments of 1500, 350, and 1950 Nm and corner frequencies of 1.69, 2.41, and 1.97 kHz which resulted in error of 6.2%, 6.6%, and 5.2%, respectively. The experimental setup invalidates several assumptions from a Brune-type source and Madariaga spectral stress drop models (Brune, 1970; Madariaga, 1976; Kaneko and Shearer, 2014, 2015), such as a circular crack, constant rupture velocity, constant stress drop, and a fully confined rupture. For this reason, we do not calculate spectral stress drop.

3.2 Spatial heterogeneity of high frequency radiation

Not only did the amplitude of high frequency energy vary, but the spatial-temporal patterns of high frequency radiation also varied with bump prominence and event type. Figure 3 shows co-located apparent slip and high-pass filtered PZ data for the three representative events as a function of space and time. PZ data from each sensor has been filtered with a 0.5 MHz

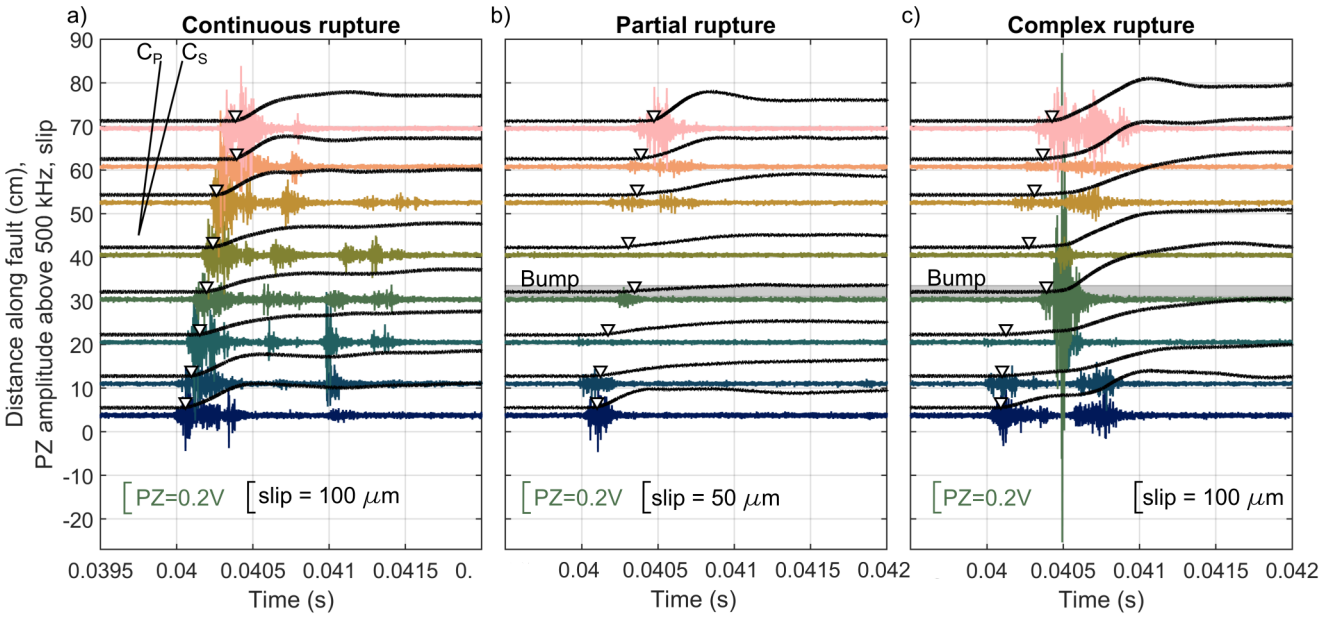

Figure 3 A 0.025 s window of three events shown in Figure 1, continuous (a), partial (b), and complex (c). Ground motions greater than 500 kHz measured by each piezo sensor overlaid with slip measurements. PZ signals are offset by sensor distance along the fault slip measurements are offset from PZ measurements for clarity. Triangles indicate the onset of slip, determined using a simple 1.2 µm threshold. a) shows the P and S wave speeds for reference. b) and c) have a grey rectangle at x = 30 cm indicating the section of the fault with locally high normal stress due to a bump.

high-pass Butterworth filter. This high-pass filter was chosen so that waveforms shown primarily result from sources that emanated directly from the nearby fault, since longer propagation distances lack such high frequencies due to attenuation in the sample. In all cases, high frequency radiation generally followed the rupture front and coincided with an increase in slip rate.

The continuous rupture had the most uniform burst of high frequency radiation associated with the primary rupture front (Figure 3a). As each fault patch began to slip (indicated by an increase in slip shown with the black line) it emitted energy. The amplitude of the emitted energy remained constant along the entire fault and always occurred simultaneously with an increase in slip. Behind the primary rupture front, additional energy is emitted, likely due to smaller, secondary rupture fronts created by free surface effects at the edge of the sample. The amplitude and duration of the PZ measurements of the main rupture front are roughly consistent across all sensors.

The partial rupture (Figure 3b) did not have a smooth, continuous rupture front as indicated by both the slip and PZ sensors. Additionally, details of the PZ and slip measurements are complicated. PZ sensors first measured a signal around x = 22 cm then show a front that propagated towards x = 0 cm. Slip sensors did not detect a change in displacement until 0.07 ms later which means the rupture initially slipped less than the noise levels on the sensors (0.4 micron) and/or the rupture did not slip the top of the fault. Slip measurements were first made on at x = 0 cm. At this point slip increased rapidly due to the sample edge effect and propagated towards the center of the fault (positive x-direction). The radiated energy increased with the rupture front. The rupture terminated at the bump however, slip reinitiated beyond the bump at x = 40 cm due to an increase in shear stress from the terminated rupture. This second rupture propagated outward in the positive x-direction and emitted a small amount of energy. When the rupture front reached the free surface at x = 74 cm, slip increased rapidly and another burst of energy was radiated. The bump never slipped and radiated energy measured near the bump was low.

The complex rupture (Figure 3c) began very similar to the partial rupture (Figure S8), the entire fault slipped while the bump remained locked. However, once the rupture had propagated through x = 74 cm, the bump slipped and released a large burst of energy, approximately five times larger than any other location on the fault. This burst of energy was spatially and temporally correlated with an increase in slip rate. Additionally, Cebry et al. (2023) observed that local stress drop on the bump was 3 MPa while local stress drop on the rest of the fault was less than 0.5 MPa. The complex slip pattern corresponded with heterogeneous high frequency radiation. This was observed at all $\overline{\sigma_n}$ levels, but was most pronounced in experiments with $\Delta\sigma_b/\overline{\sigma_n}$ greater than 6.

4 Discussion

4.1 Source Model

We found that a Brune-type source model provides a reasonable fit to the source spectra (Figure S7). The source spectra are depleted around the corner frequency as has been observed in other laboratory studies (McLaskey et al., 2015; Selvadurai, 2019). Unlike other laboratory studies, the model is best fit by a high

frequency fall off of ω^{-1} despite a fast rupture velocity. One possible reason is due to assumptions in the Brune source model. Our ruptures have a larger length to width ratio than those in McLaskey et al. (2015), Selvadurai (2019), and Wu and McLaskey (2019) so deviation from the circular source model may effect our model results more than previous studies. Our ruptures are also unconfined, unlike those Selvadurai (2019) and Wu and McLaskey (2019), which has been shown to affect source parameters (Steinhardt et al., 2023).

Another possibility is that our source spectra is best fit by a double-corner frequency model (Figure S7) as seen for other more complex ruptures with multiple asperities or rupture phases. For example, Boatwright (1988) considered a "sub-event" or "asperity" model and found composite event radiation was represented by the sum of the sub-events. The resulting spectra had two corner frequencies, one related to the entire event and another related to the individual sub-events. Ji and Archuleta (2021) applied the double-corner frequency model to many natural events and found that models better reproduced the PGA for these events since the double-corner model allows for the possibility that the stress drop is not uniform within the ruptured region. This is certainly the case with our complex ruptures. It is plausible that a second corner frequency is above the frequency range we measured ($>10^5$ Hz) and a double corner frequency model would be better applicable to these events.

4.2 Complex radiation patterns

These experiments demonstrate how a single normal stress bump can create complex ruptures with heterogeneous seismic radiation patterns. On a fault without a bump, high frequency radiation followed the rupture tip and radiated uniformly as the rupture propagated along the simulated fault. Rupture propagated at a nearly constant rate of 2100 m/s, between the P and S wave speed of PMMA (2.7 and 1.4 km/s), in agreement with previous observations of supershear ruptures on plastic laboratory faults (Xia et al., 2004; Ben-David et al., 2010; Rubino et al., 2017; Dong et al., 2023). Faults with a bump had a larger variance in rupture speed, with some patches of the fault approaching supershear while others remained subshear. For the complex rupture, measured high frequency radiation varied by nearly an order-of-magnitude depending on the observation location. The bump radiated the most high frequency energy when it slipped, while neighboring, low stress regions, emitted much less for the same rupture event. Overall rupture velocity that we could observe did not correlate with near-field PGA. The complex rupture had higher or similar near-field PGA compared to the continuous event. Supershear events are known to radiate strong seismic waves (Dunham and Archuleta, 2005; Andrews, 2010) and yet the bump radiated an order-of-magnitude larger near-field PGA.

In all cases, we can link seismic radiation to slip rate. Peak slip rate, measured from displacement sensors co-located with piezoelectric sensors, is spatially correlated with near-field PGA (Figure 4). Stress drop measurements of a complex event from Cebry et al. (2023) show that local stress drop on the bump was at least six times that of the rest of the fault and is spatially correlated with large near-field PGA. While we do not have shear stress measurements for continuous and partial rupture, we expect this correlation to hold.

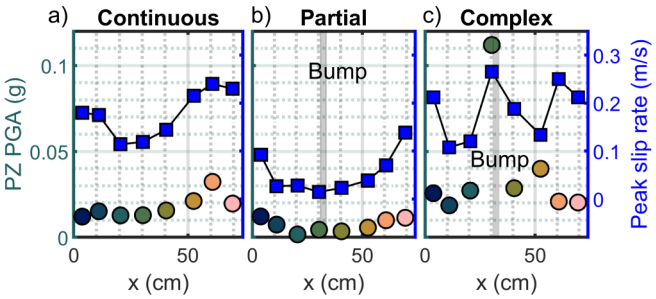

Figure 4 Near-field peak ground acceleration shown in colored circles and peak slip rate marked by blue squares for each of the three events shown in Figure 1 continuous (a), partial (b), and complex (c). b) and c) have a grey rectangle at x = 30 cm indicating the section of the fault with locally high normal stress due to a bump.

Conceptually, we can explain the enhanced high frequency energy by considering the locked patches as small areas with locally high stress capacity, similar to some earthquake gates (Oskin et al., 2015; Duan et al., 2019). When these patches slip, a large amount stress is relieved (Dunham et al., 2003; Cebry et al., 2023). The large stress drop will result in an increased amplitude of the radiated waves from that patch (e.g., Ozacar and Beck, 2004). Assuming the patches are small relative to the entire ruptured area, the corner frequency or the radiated spectra nearest the bump will be higher than the spatial average corner frequency (i.e., $f_{c,bump} > f_{c,average}$) such that the bump contributes more to the high frequency energy than the rest of the fault.

4.3 Comparison to natural events

Natural faults have geometric heterogeneities from multi-scale roughness, branches, and stepovers (Cochran et al., 2023; Candela and Brodsky, 2016; Sagy et al., 2007). There are also observations of geographical areas with spatially coherent stress drops and PGA (Trugman and Shearer, 2017). Geometrical heterogeneities are expected to persist over several earthquake cycles, which would create regions with persistently high stress drop and PGA. In our study, we only consider a single bump which greatly simplified our results (Figure 5b), yet still produced a large range of PGA over sequences of multiple events. We also expect that heterogeneities at all scales can enhance high frequency energy to some degree, based on our observations of enhanced high frequency energy even when the bump did not stop rupture (Figure S6). This is supported by modeling studies that have shown that enhanced high frequency radiation is expected to persist even for multiple or small heterogeneities (Oral et al., 2022; Madariaga et al., 2006; Das and Aki, 1977; Dunham et al., 2011; Shi and Day, 2013).

To illustrate the potential level of complexity on natural faults, we estimated a normal stress distribution due to slip on a fault with a synthetic roughness profile (Figure 5c). A spatial spectral fall off of 1.4 was used to characterise the fault roughness in line with natural measurements (Beeler, 2021). The normal stress distribution was then calculated from the spatial derivative of the roughness profile (Fang and Dunham, 2013; Cattania and Segall, 2021). These stress heterogeneities may result in a very complex PGA both within individual events and across sequences of earthquakes.

When natural ruptures can encounter multiple bumps, kinks, or other barriers (Rodriguez Padilla et al., 2022) they may terminate differently depending on strength excess (Boatwright and Quin, 1986; Cebry et al., 2023). This adds another layer of difficulty to accurately predict high frequency ground motions (Figure 5). Radiated spectra of small events, in addition to details such as timing and location, may help identify fault structure or stress state and provide insight into the expected spatial distribution of PGA in future large earthquakes.

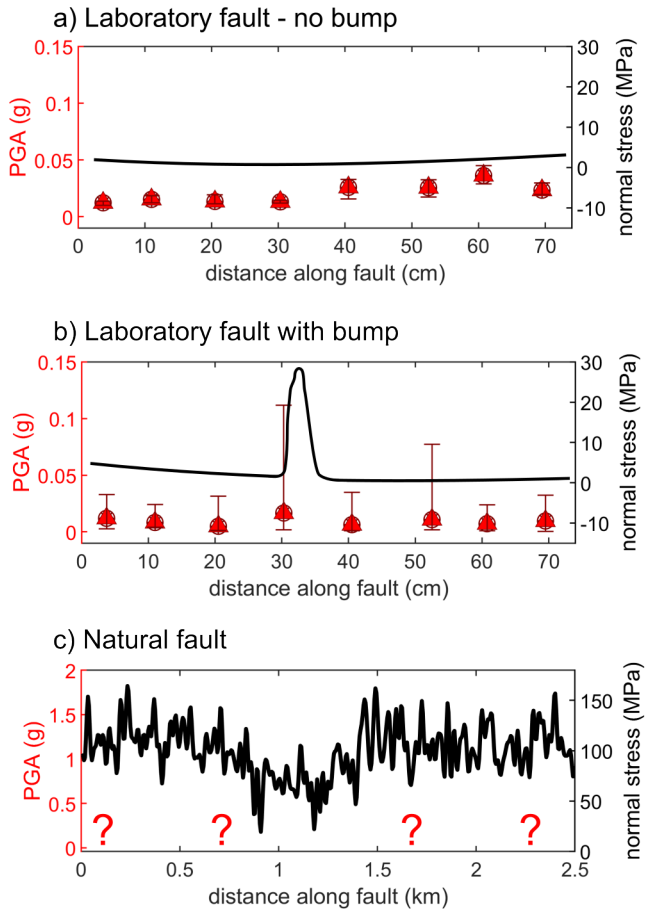

Figure 5 Normal stress (black) and PGA (red) along fault length for (a) a laboratory fault without a bump, (b) a laboratory fault with a bump, and (c) a natural fault. Red triangles indicate the PGA averaged across all events in the experimental run. Bars at each point indicate the maximum and minimum PGA from any event in the experimental run measured at each location. Normal stress due to slip on a natural fault is determined based on a synthetic roughness profile. Question marks in (c) indicate a knowledge gap.

We compare our results to observations of heterogeneous PGA during the 2023 M_w 7.8 and M_w 7.6 Kahramanmaraş earthquakes on the Eastern Anatolian fault system in Turkey, although this is by no means the only observation of heterogeneous ground motions (Bakun et al., 2005; Loh et al., 2000; Lee et al., 2007). During the M_w 7.8, PGA locally reached 2g on some sections of the ruptured Anatolian fault, while others remained below 0.5 g (Mai et al., 2023). PGA measurements are affected by several factors including site and soil effects, rupture geometry, and heterogeneity of fault slip. However, there is evidence that geometric barriers resulted in a complex rupture with multiple subevents (Jia et al., 2023; Zhang et al., 2023; Sagy et al., 2024). Zhang et al. (2023) further showed that the branching junctions on the East Anatolian fault radiated enhanced high frequency waves. It is plausible that the junctions acted as strong patches on the Anatolian fault. When these strong patches slipped, a large amount of stress was quickly released which resulted in the surrounding area experiencing a burst of high radiated energy and high PGAs, similar to our experiments (Figure 5).

5 Conclusions

In these experiments, we added a bump of locally high normal stress to an otherwise uniform fault, which resulted in complex ruptures with enhanced high frequency radiation relative to low frequency radiation. High frequency energy and PGA were spatially heterogeneous in experiments with a bump. Experiments without a bump produced smooth, continuous ruptures which had lower high frequency energy. In this case, high frequency energy was spatially uniform. PGA was overall higher for complex ruptures than continuous ruptures despite a slower, sub-supershear rupture velocity.

Variations in high frequency energy were spatially and temporally correlated with sudden increases in slip velocity and local stress drop. When the rupture propagated smoothly, such as in the continuous rupture case, the radiated high frequency energy had spatially consistent amplitude and timing. When the rupture propagated in a complex multi-phase rupture due to a high normal stress bump, the high frequency energy was spatially heterogeneous, with the largest PGA measured near the bump. We propose that geometrical heterogeneities may be a plausible explanation for natural observations of variations in near fault PGA, such as during the 2023 Kahramanmaraş M_w 7.8 and 7.6 earthquakes. Since the heterogeneities are the result of structural features, large PGA during one earthquake would be a strong predictor of large PGA in the same location during a subsequent earthquake rupturing the same fault section.

Acknowledgements

The authors gratefully acknowledge that this work was funded by National Science Foundation grant EAR-1847139 and EAR-2240375. We also thank Kian Sorhaindo for building the samples and Jim Strait for

technical assistance. We are incredibly grateful to Coralis Del Mar Friedman-Álvarez and Carolina Muñoz-Saez for their work translating the abstract and non-technical summary. The authors would also like to acknowledge Matt Ikari for handling the review of this paper and the thoughtful feedback from Marco Scuderi and an anonymous reviewer which enhanced this paper. Data reported in this paper were acquired from laboratory experiments conducted at Cornell University.

Data and code availability

Data are available through Cornell eCommons at https://doi.org/10.7298/s53e-vy26.

Competing interests

The authors have no competing interests.

References

Andrews, D. J. Ground motion hazard from supershear rupture. *Tectonophysics*, 493(3):216–221, Oct. 2010. doi: 10.1016/j.tecto.2010.02.003.

Bakun, W. H., Aagaard, B., Dost, B., Ellsworth, W. L., Hardebeck, J. L., Harris, R. A., Ji, C., Johnston, M. J. S., Langbein, J., Lienkaemper, J. J., Michael, A. J., Murray, J. R., Nadeau, R. M., Reasenberg, P. A., Reichle, M. S., Roeloffs, E. A., Shakal, A., Simpson, R. W., and Waldhauser, F. Implications for prediction and hazard assessment from the 2004 Parkfield earthquake. *Nature*, 437(7061):969–974, Oct. 2005. doi: 10.1038/nature04067.

Bao, H., Ampuero, J.-P., Meng, L., Fielding, E. J., Liang, C., Milliner, C. W. D., Feng, T., and Huang, H. Early and persistent supershear rupture of the 2018 magnitude 7.5 Palu earthquake. *Nature Geoscience*, 12(3):200–205, Mar. 2019. doi: 10.1038/s41561-018-0297-z.

Beeler, N. M. Characterizing fault roughness—Are faults rougher at long or short wavelengths? Open-file report 2020-1134, US Geological Survey, 2021. doi: 10.3133/ofr20201134.

Ben-David, O., Cohen, G., and Fineberg, J. The Dynamics of the Onset of Frictional Slip. *Science*, 330(6001):211–214, Oct. 2010. doi: 10.1126/science.1194777.

Boatwright, J. The seismic radiation from composite models of faulting. *Bulletin of the Seismological Society of America*, 78(2): 489–508, Apr. 1988. doi: 10.1785/BSSA0780020489.

Boatwright, J. and Quin, H. The Seismic Radiation from a 3-D Dynamic Model of a Complex Rupture Process. Part I: Confined Ruptures. In *Earthquake Source Mechanics*, pages 97–109. American Geophysical Union (AGU), 1986. doi: https://doi.org/10.1029/GM037p0097.

Brune, J. N. Tectonic stress and the spectra of seismic shear waves from earthquakes. *Journal of Geophysical Research*, 75(26): 4997–5009, Sept. 1970. doi: 10.1029/JB075i026p04997.

Buijze, L., Guo, Y., Niemeijer, A., Ma, S., and Spiers, C. Effects of heterogeneous gouge segments on the slip behavior of experimental faults at dm scale. *Earth and Planetary Science Letters*, 554:116652, Jan. 2021. doi: 10.1016/j.epsl.2020.116652.

Candela, T. and Brodsky, E. E. The minimum scale of grooving on faults. *Geology*, 44(8):603–606, Aug. 2016. doi: 10.1130/G37934.1.

Cattania, C. and Segall, P. Precursory Slow Slip and Foreshocks on Rough Faults. *Journal of Geophysical Research: Solid Earth*, 126(4):e2020JB020430, 2021. doi: https://doi.org/10.1029/2020JB020430.

Cebry, S. B. L., Ke, C.-Y., and McLaskey, G. C. The Role of Background Stress State in Fluid-Induced Aseismic Slip and Dynamic Rupture on a 3-m Laboratory Fault. *Journal of Geophysical Research: Solid Earth*, 127(8):e2022JB024371, 2022a. doi: 10.1029/2022JB024371.

Cebry, S. B. L., Ke, C.-Y., Shreedharan, S., Marone, C., Kammer, D. S., and McLaskey, G. C. Creep fronts and complexity in laboratory earthquake sequences illuminate delayed earthquake triggering. *Nature Communications*, 13(1):6839, Nov. 2022b. doi: 10.1038/s41467-022-34397-0.

Cebry, S. B. L., Sorhaindo, K., and McLaskey, G. C. Laboratory Earthquake Rupture Interactions With a High Normal Stress Bump. *Journal of Geophysical Research: Solid Earth*, 128(11): e2023JB027297, Nov. 2023. doi: 10.1029/2023JB027297.

Cochran, E. S., Page, M. T., Van Der Elst, N. J., Ross, Z. E., and Trugman, D. T. Fault Roughness at Seismogenic Depths and Links to Earthquake Behavior. *The Seismic Record*, 3(1):37–47, Jan. 2023. doi: 10.1785/0320220043.

Courboulex, F., Dujardin, A., Vallee, M., Delouis, B., Sira, C., Deschamps, A., Honore, L., and Thouvenot, F. High-Frequency Directivity Effect for an Mw 4.1 Earthquake, Widely Felt by the Population in Southeastern France. *Bulletin of the Seismological Society of America*, 103(6):3347–3353, Dec. 2013. doi: 10.1785/0120130073.

Das, S. and Aki, K. Fault plane with barriers: A versatile earthquake model. *Journal of Geophysical Research*, 82(36):5658–5670, Dec. 1977. doi: 10.1029/JB082i036p05658.

Dong, P., Xia, K., Xu, Y., Elsworth, D., and Ampuero, J.-P. Laboratory earthquakes decipher control and stability of rupture speeds. *Nature Communications*, 14(1):2427, Apr. 2023. doi: 10.1038/s41467-023-38137-w.

Duan, B., Liu, Z., and Elliott, A. J. Multicycle Dynamics of the Aksay Bend Along the Altyn Tagh Fault in Northwest China: 2. The Realistically Complex Fault Geometry. *Tectonics*, 38(3):1120–1137, Mar. 2019. doi: 10.1029/2018TC005196.

Dunham, E. M. and Archuleta, R. J. Near-source ground motion from steady state dynamic rupture pulses. *Geophysical Research Letters*, 32(3), Feb. 2005. doi: 10.1029/2004GL021793.

Dunham, E. M., Favreau, P., and Carlson, J. M. A Supershear Transition Mechanism for Cracks. *Science*, 299(5612):1557–1559, Mar. 2003. doi: 10.1126/science.1080650.

Dunham, E. M., Belanger, D., Cong, L., and Kozdon, J. E. Earthquake Ruptures with Strongly Rate-Weakening Friction and Off-Fault Plasticity, Part 2: Nonplanar Faults. *Bulletin of the Seismological Society of America*, 101(5):2308–2322, Oct. 2011. doi: 10.1785/0120100076.

Fang, Z. and Dunham, E. M. Additional shear resistance from fault roughness and stress levels on geometrically complex faults. *Journal of Geophysical Research: Solid Earth*, 118(7):3642–3654, 2013. doi: https://doi.org/10.1002/jgrb.50262.

Ji, C. and Archuleta, R. J. Two Empirical Double-Corner-Frequency Source Spectra and Their Physical Implications. *Bulletin of the Seismological Society of America*, 111(2):737–761, Apr. 2021. doi: 10.1785/0120200238.

Jia, Z., Jin, Z., Marchandon, M., Ulrich, T., Gabriel, A.-A., Fan, W., Shearer, P., Zou, X., Rekoske, J., Bulut, F., Garagon, A., and Fialko, Y. The complex dynamics of the 2023 Kahramanmaraş, Turkey, M_w 7.8-7.7 earthquake doublet. *Science*, 381(6661): 985–990, Sept. 2023. doi: 10.1126/science.adi0685.

Kaneko, Y. and Shearer, P. M. Seismic source spectra and estimated stress drop derived from cohesive-zone models of circu-

lar subshear rupture. *Geophysical Journal International*, 197(2): 1002–1015, May 2014. doi: 10.1093/gji/ggu030.

Kaneko, Y. and Shearer, P. M. Variability of seismic source spectra, estimated stress drop, and radiated energy, derived from cohesive-zone models of symmetrical and asymmetrical circular and elliptical ruptures. *Journal of Geophysical Research: Solid Earth*, 120(2):1053–1079, Feb. 2015. doi: 10.1002/2014JB011642.

Lee, S.-J., Chen, H.-W., and Ma, K.-F. Strong ground motion simulation of the 1999 Chi-Chi, Taiwan earthquake from a realistic three-dimensional source and crustal structure. *Journal of Geophysical Research: Solid Earth*, 112(B6), 2007. doi: https://-doi.org/10.1029/2006JB004615.

Loh, C.-H., Lee, Z.-K., Wu, T.-C., and Peng, S.-Y. Ground motion characteristics of the Chi-Chi earthquake of 21 September 1999. *Earthquake Engineering & Structural Dynamics*, 29 (6):867–897, 2000. doi: https://doi.org/10.1002/(SICI)1096-9845(200006)29:6<867::AID-EQE943>3.0.CO;2-E.

Madariaga, R. Dynamics of an expanding circular fault. *Bulletin of the Seismological Society of America*, 66(3):639–666, June 1976. doi: 10.1785/BSSA0660030639.

Madariaga, R., Ampuero, J. P., and Adda-Bedia, M. Seismic radiation from simple models of earthquakes. *Geophysical Monograph Series*, 170:223–236, 2006. doi: 10.1029/170GM23.

Mai, P. M., Aspiotis, T., Aquib, T. A., Cano, E. V., Castro-Cruz, D., Espindola-Carmona, A., Li, B., Li, X., Liu, J., Matrau, R., Nobile, A., Palgunadi, K. H., Ribot, M., Parisi, L., Suhendi, C., Tang, Y., Yalcin, B., Avşar, U., Klinger, Y., and Jónsson, S. The Destructive Earthquake Doublet of 6 February 2023 in South-Central Türkiye and Northwestern Syria: Initial Observations and Analyses. *The Seismic Record*, 3(2):105–115, Apr. 2023. doi: 10.1785/0320230007.

Marty, S., Passelègue, F. X., Aubry, J., Bhat, H. S., Schubnel, A., and Madariaga, R. Origin of High-Frequency Radiation During Laboratory Earthquakes. *Geophysical Research Letters*, 46(7): 3755–3763, Apr. 2019. doi: 10.1029/2018GL080519.

McLaskey, G. C. and Glaser, S. D. Hertzian impact: Experimental study of the force pulse and resulting stress waves. *The Journal of the Acoustical Society of America*, 128(3):1087–1096, Sept. 2010. doi: 10.1121/1.3466847.

McLaskey, G. C. and Lockner, D. A. Shear failure of a granite pin traversing a sawcut fault. *International Journal of Rock Mechanics and Mining Sciences*, 110:97–110, Oct. 2018. doi: 10.1016/j.ijrmms.2018.07.001.

McLaskey, G. C. and Yamashita, F. Slow and fast ruptures on a laboratory fault controlled by loading characteristics. *Journal of Geophysical Research: Solid Earth*, 122(5):3719–3738, May 2017. doi: 10.1002/2016JB013681.

McLaskey, G. C., Lockner, D. A., Kilgore, B. D., and Beeler, N. M. A Robust Calibration Technique for Acoustic Emission Systems Based on Momentum Transfer from a Ball Drop. *Bulletin of the Seismological Society of America*, 105(1):257–271, Feb. 2015. doi: 10.1785/0120140170.

Miyake, H. Source Characterization for Broadband Ground-Motion Simulation: Kinematic Heterogeneous Source Model and Strong Motion Generation Area. *Bulletin of the Seismological Society of America*, 93(6):2531–2545, Dec. 2003. doi: 10.1785/0120020183.

Oral, E., Ampuero, J. P., Ruiz, J., and Asimaki, D. A Method to Generate Initial Fault Stresses for Physics-Based Ground-Motion Prediction Consistent with Regional Seismicity. *Bulletin of the Seismological Society of America*, 112(6):2812–2827, Dec. 2022. doi: 10.1785/0120220064.

Oskin, M. E., Elliott, A. J., Duan, B., Lui-Zeng, J., Lui, Z., Shao, Y., and et, a. Earthquake gates: Linking rupture length to geologically constrained dynamics of fault complexity, with examples from the Altyn Tagh and San Andreas faults. In *Earthquake gates: Linking rupture length to geologically constrained dynamics of fault complexity, with examples from the Altyn Tagh and San Andreas faults*, Baltimore, MD, Nov. 2015.

Ozacar, A. A. and Beck, S. L. The 2002 Denali Fault and 2001 Kunlun Fault Earthquakes: Complex Rupture Processes of Two Large Strike-Slip Events. *Bulletin of the Seismological Society of America*, 94(6B):S278–S292, Dec. 2004. doi: 10.1785/0120040604.

Rodriguez Padilla, A. M., Oskin, M. E., Rockwell, T. K., Delusina, I., and Singleton, D. M. Joint earthquake ruptures of the San Andreas and San Jacinto faults, California, USA. *Geology*, 50(4): 387–391, Apr. 2022. doi: 10.1130/G49415.1.

Rousseau, C.-E. and Rosakis, A. J. On the influence of fault bends on the growth of sub-Rayleigh and intersonic dynamic shear ruptures: INFLUENCE OF FAULTS BENDS ON SHEAR RUPTURES. *Journal of Geophysical Research: Solid Earth*, 108(B9), Sept. 2003. doi: 10.1029/2002JB002310.

Rubino, V., Rosakis, A. J., and Lapusta, N. Understanding dynamic friction through spontaneously evolving laboratory earthquakes. *Nature Communications*, 8(1):15991, June 2017. doi: 10.1038/ncomms15991.

Rubino, V., Lapusta, N., and Rosakis, A. J. Intermittent lab earthquakes in dynamically weakening fault gouge. *Nature*, 606 (7916):922–929, June 2022. doi: 10.1038/s41586-022-04749-3.

Sagy, A., Brodsky, E. E., and Axen, G. J. Evolution of fault-surface roughness with slip. *Geology*, 35(3):283–286, Mar. 2007. doi: 10.1130/G23235A.1.

Sagy, A., Morad, D., and Lyakhovsky, V. Can Geometrical Barrier Explain the Mw 7.8 Earthquake in Southern Türkiye on February 2023? *Seismological Research Letters*, 95(2A):643–650, Jan. 2024. doi: 10.1785/0220230280.

Selvadurai, P. A. Laboratory Insight Into Seismic Estimates of Energy Partitioning During Dynamic Rupture: An Observable Scaling Breakdown. *Journal of Geophysical Research: Solid Earth*, 124(11):11350–11379, Nov. 2019. doi: 10.1029/2018JB017194.

Shi, Z. and Day, S. M. Rupture dynamics and ground motion from 3-D rough-fault simulations. *Journal of Geophysical Research: Solid Earth*, 118(3):1122–1141, Mar. 2013. doi: 10.1002/j-grb.50094.

Steinhardt, W., Dillavou, S., Agajanian, M., Rubinstein, S. M., and Brodsky, E. E. Seismological Stress Drops for Confined Ruptures Are Invariant to Normal Stress. *Geophysical Research Letters*, 50 (9):e2022GL101366, May 2023. doi: 10.1029/2022GL101366.

Trugman, D. T. and Shearer, P. M. Application of an improved spectral decomposition method to examine earthquake source scaling in Southern California. *Journal of Geophysical Research: Solid Earth*, 122(4):2890–2910, Apr. 2017. doi: 10.1002/2017JB013971.

Tsurugi, M., Tanaka, R., Kagawa, T., and Irikura, K. High-Frequency Spectral Decay Characteristics of Seismic Records of Inland Crustal Earthquakes in Japan: Evaluation of the fmax and κ Models. *Bulletin of the Seismological Society of America*, 110(2): 452–470, Mar. 2020. doi: 10.1785/0120180342.

Wu, B. S. and McLaskey, G. C. Broadband Calibration of Acoustic Emission and Ultrasonic Sensors from Generalized Ray Theory and Finite Element Models. *Journal of Nondestructive Evaluation*, 37(1):8, Mar. 2018. doi: 10.1007/s10921-018-0462-8.

Wu, B. S. and McLaskey, G. C. Contained Laboratory Earthquakes Ranging From Slow to Fast. *Journal of Geophysical Research: Solid Earth*, 124(10):10270–10291, Oct. 2019. doi: 10.1029/2019JB017865.

Xia, K., Rosakis, A. J., and Kanamori, H. Laboratory Earthquakes:

The Sub-Rayleigh-to-Supershear Rupture Transition. *Science*, 303(5665):1859–1861, Mar. 2004. doi: 10.1126/science.1094022.

Yamashita, F., Fukuyama, E., Xu, S., Kawakata, H., Mizoguchi, K., and Takizawa, S. Two end-member earthquake preparations illuminated by foreshock activity on a meter-scale laboratory fault. *Nature Communications*, 12(1):4302, July 2021. doi: 10.1038/s41467-021-24625-4.

Zhang, Y., Tang, X., Liu, D., Taymaz, T., Eken, T., Guo, R., Zheng, Y., Wang, J., and Sun, H. Geometric controls on cascading rupture of the 2023 Kahramanmaraş earthquake doublet. *Nature Geoscience*, 16(11):1054–1060, Nov. 2023. doi: 10.1038/s41561-023-01283-3.